Self-consistent model of a direct-current glow discharge: Treatment of fast electrons

M. Surendra, D. B. Graves, and G. M. Jellum
Department of Chemical Engineering, University of California, Berkeley, Berkeley, California 94720
(Received 3 April 1989; revised manuscript received 21 August 1989)

Mathematical models of dc glow discharges sustained by electrons emitted by the cathode and accelerated into the cathode fall must take into account the highly nonequilibrium nature of these fast electrons. However, the electric field profile through the discharge is determined mainly by the distribution of ions and slow electrons. In this paper we explore three methods to account for fast, nonequilibrium electrons: the single-beam method, the multibeam method, and particle (Monte Carlo) simulations. Ions and cold electrons are treated using equations of change assuming collisionally dominated motion (i.e., drift and diffusion), and the self-consistent electric field is determined by solving these equations simultaneously with Poisson's equation. Creation rates for ions and slow electrons are obtained from the fast-electron models. Simulation results indicate that, although the single-beam model is qualitatively correct, it is hampered by its sensitivity to assumptions in the numerical approach, and its tendency to predict negative voltage-current characteristics at low pressures and high voltages, which are not evident in results from the higher-order multibeam model. Although an improvement over the single-beam model, comparison with experimental optical-emission measurements reveals that the multibeam model predicts excitation profiles that extend too far into the discharge. Accurate comparisons are possible with particle simulations, which incorporate angular scattering of fast electrons.

I. INTRODUCTION

Direct-current (dc) cold-cathode glow discharges have been studied for many years.[1] Recently, efforts have intensified to understand the cathode fall and negative glow regions of dc discharges. These efforts have included both experimental[2–5] and theoretical treatments.[5–8] The most dramatic advances experimentally have come about with the application of laser diagnostics to probe electric field strength profiles, ion densities, species energy distributions, etc. Theoretical treatments have focused on appropriate ways to handle the highly nonequilibrium nature of electron transport in the cathode fall where the electric field strengths are much larger than in other parts of the discharge. Although it has long been recognized that some form of kinetic theory treatment is necessary to account rigorously for the behavior of energetic electrons that originate in the cathode-fall region and subsequently traverse the negative glow, it has proven difficult to make the kinetic theory models self-consistent. Two major approaches have been used to model dc glows. One is a self-consistent treatment based on the moments of the Boltzmann equation coupled with Poisson's equation.[9–12] The other is a kinetic approach, either Boltzmann,[13,14] or Monte Carlo.[15–19] This approach, however, has required the use of an assumed electric field profile. Recent work in self-consistent kinetic models of the cathode fall have been successful.[7] Nonetheless, these calculations have not been extended self-consistently through the negative glow to the anode.

This paper describes an approach to the problem of accounting for fast, highly nonequilibrium electrons that originate in the cathode fall, as well as calculating the self-consistent electric field profile from Poisson's equation. The basic ideas are best illustrated by reference to Fig. 1, which is a schematic of a cold-cathode dc glow discharge. The discharge is sustained by emission of secondary electrons from the cathode due primarily to positive ion bombardment. The secondary electrons are accelerated in the cathode fall to high energies and ionize neutrals there. The electrons thus created are also accelerated and an ionization cascade forms. Because at high energies electrons tend to forward scatter, the energetic electrons continue to propagate into the low-field region of the discharge, resulting in ionization and electronic excitation throughout the discharge gap. The fast or energetic electrons are present in relatively low concentrations compared to the low energy, but far more numerous, slow or "bulk" electrons in the quasineutral region. These electrons have energies that are typically in the range of 0.1–0.5 eV, and therefore cannot be responsible for the majority of inelastic collisions. They are important for space charge and ambipolar diffusion, however, which help determine the ion density profile. The goal of our mathematical model is to represent these processes in a relatively simple, but physically reasonable fashion. The key is to break the electrons up into two groups: the fast electrons that originate as secondary electrons at the cathode surface or are created primarily in the ionization cascade in the cathode-fall region are treated as one group; and the slow, bulk electrons that reside in the quasineutral region of the discharge are a second group.[8]

The first part of this paper is an exploration of two beam approaches for modeling the hot electrons that originate in the cathode fall: the single (or monoenergetic) beam and the multibeam models. In the single-beam

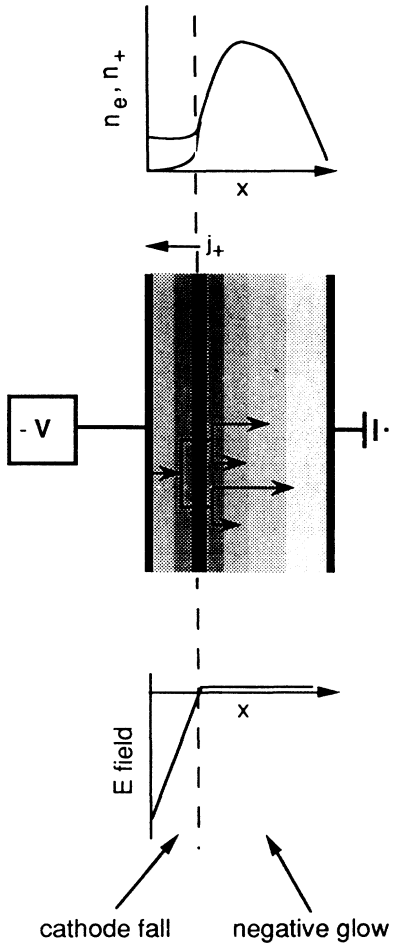

FIG. 1. Schematic of a dc discharge with typical density and electric field profiles. The shading intensity represents the intensity of light emission in the discharge.

model, energetic electrons are treated as if they all had the same energy at a given position in the discharge.[6,8,20,21] A multibeam model allows for a distribution of hot electron energies, which is more realistic since not all electrons fall across the same voltage or experience the same collisional energy losses.[21–25] In the latter half of the paper we report on work treating fast electrons as individual particles, following their motion using a Monte Carlo approach. By treating only fast electrons as particles and slow electrons and ions as fluids, we are able to obtain self-consistent simulations of the entire discharge while accounting for the highly nonequilibrium nature of hot electron motion throughout the discharge. Experimental optical-emission measurements are also shown for comparison with multibeam and particle simulation results.

II. MATHEMATICAL MODEL

A. Model assumptions

The gas is assumed to be weakly ionized and at room temperature. The model system is a discharge between two infinitely wide electrodes, so that quantities vary only with distance between electrodes. Although in principle our model formulation is capable of describing a positive column as well as the negative glow, we consider only cases in which electrode separation is small enough to prevent the formation of a positive column. The discharge is assumed to consist of four species: neutral, ground-state argon atoms at room temperature; positive ions; slow electrons; and fast electrons.

Additional assumptions include the following.

(1) Only electron-impact ionization and excitation from the ground-state neutral are included as inelastic electron-neutral collisions. To further simplify matters, we have combined all the various excitation processes for argon into one composite excitation process which has a threshold energy of 12 eV. The model can be adapted to include effects such as two-step ionization or excitation involving the metastable states by the addition of the appropriate balance equations and rates.

(2) Only one type of ionic species (Ar^+) is considered. The presence of molecular ions (e.g., Ar_2^+) can be included with the appropriate conservation equations and rates.

(3) Ion and slow-electron motion is assumed to be collisionally dominated (i.e., the collision frequency of charged particles with neutrals is much larger than the gradient of the species velocity). Hence the momentum balance equations reduce to expressions involving only drift and diffusion. The assumption is valid for the slow-electron group as they exist only in the low electric field region. Furthermore, Boltzmann equation calculations by Lawler[26] indicate that ions (dominated by charge exchange collisions) equilibrate relatively quickly in the cathode fall.

(4) Neutral gas density and composition are uniform throughout the discharge.

B. Fluid model

The fluid model has been used extensively to model dc and rf glows.[10,11,27–29] It consists of conservation equations for ions and electrons (slow electrons in this case), and Poisson's equation for a self-consistent electric field:

$$\frac{\partial n_e}{\partial t}+\frac{\partial j_e}{\partial x}=C_e \ , \tag{1}$$

$$\frac{\partial n_+}{\partial t}+\frac{\partial j_+}{\partial x}=C_+ \ , \tag{2}$$

$$\frac{\partial^2 V}{\partial x^2}+\frac{e}{\varepsilon_0}(n_+-n_e-n_{be})=0 \ , \tag{3}$$

$$j_e=\mu_e n_e\frac{\partial V}{\partial x}-D_e\frac{\partial n_e}{\partial x} \ , \tag{4}$$

$$j_+=-\mu_+ n_+\frac{\partial V}{\partial x}-D_+\frac{\partial n_+}{\partial x} \ . \tag{5}$$

Equation (1) is the slow-electron conservation equation, where n_e is the slow-electron density, j_e is the slow-electron flux, and C_e is the slow-electron creation rate. j_e is expressed as the sum of drift and diffusion [Eq. (4)], where μ_e is the slow-electron mobility, and D_e is the slow-electron diffusivity. Both parameters are functions

of electron energy. However, we have taken the parameters to be constant. Equations (2) and (5) are the positive ion conservation and flux equations, respectively. The + subscript refers to positive ions. Since ion diffusion is relatively unimportant, D_+ is assumed to be constant while μ_+ is taken as function of E/n_n, where E is the electric field and n_n is the neutral number density [see Eq. (22)]. Both C_e and C_+ come from the fast-electron models (discussed in the next section). This is essentially the only coupling between the fast-electron models and the fluid model. The fluid model influences the fast-electron models through Poisson's equation and the boundary conditions. It is important to note that since there are two types of electrons, C_e is not equal to C_+. C_+ is equal to the total ionization rate, whereas C_e is zero in the cathode fall. Furthermore, C_e can be different from C_+ in the negative glow because of the contribution of the fast electrons which are lost to the slow-electron group. The details of C_+ and C_e are discussed in the next section. Equation (3) is Poisson's equation, where n_{be} is the fast-electron density. We neglect the contribution of n_{be} to the expression for charge density in Eq. (3) under the assumption that it is smaller than $(n_+ - n_e)$. This assumption is approximately valid in our calculations as the ratio of n_{be} to $(n_+ - n_e)$ is less than 0.3. Nonetheless, it should be noted that this assumption is often not valid, thus n_{be} should, in general, be retained in Eq. (3).

The three equations [Eqs. (1)–(3)] are second order in space, so two boundary conditions are required for each equation. We choose the following: at the cathode ($x=0$ mm), $j_e=0$, $\partial n_+/\partial x=0$, and $V=V_{\text{cath}}$; and at the anode ($x=20$ mm), $n_e=0$, $\partial n_+/\partial x=0$, and $V=0$.

C. Fast-electron models

Fast electrons are assumed to be completely forward scattered in all collisions in both the single- and multibeam models. This assumption greatly simplifies the solution of equations describing fast-electron number density and motion, since all fast electrons move only in the direction from cathode to anode. This makes the equations equivalent to initial value problems, requiring only a simple forward-matching integration scheme for solution. The assumption of complete forward scattering is generally justified for highly energetic electrons. In Fig. 2 we present differential cross sections $I(\varepsilon,\chi)$ (ε is the electron energy and χ is the scattering angle), for elastic scattering in argon from Vuskovic and Kurepa.[30] The data indicate that about 55% of the electrons in the energy range $\varepsilon=60-150$ eV scatter with angles less than 30°. This fraction increases with increasing electron energy.[31] [We plot a normalized version of the differential cross sections, $2\pi I(\varepsilon,\chi)\sin\chi/\sigma(\varepsilon)$, as it is then simpler to estimate the probability of scattering within a certain angle. Furthermore, the data can be readily compared with the analytic form presented in Fig. 5.] However, at low energies (~ 10 eV), large-angle scattering is significant. In these models we neglect large-angle scattering while recognizing that the assumption is not always correct.

In the beam models, we distinguish fast electrons from slow electrons based on their energy and where they are created in the discharge. The rationale for this separation is based on the difference between cathode-fall (high-field) and negative-glow (low-field) regions. Positive ions that traverse the cathode fall and impinge on the cathode cause secondary electron emission from the surface. These electrons are treated as fast electrons. At the cathode, the flux of fast electrons, j_{be}, is related to the positive ion flux, j_+, by

$$j_{be}=-\gamma j_+ , \qquad (6)$$

where γ is the secondary emission coefficient. Fast electrons avalanche in the cathode fall, creating more positive ions and fast electrons. No slow electrons are created here. However, once the fast electrons enter the negative glow, the creation of slow electrons is enabled. In the two beam models we consider, rules differ somewhat regarding creation and loss of fast and slow electrons in the low-field region of the discharge. In the single-beam model, ionization in the negative glow results only in the formation of slow electrons, whereas in the multibeam model some fast-electron creation can continue to occur. Once the fast electrons drop below some threshold energy, they enter the slow-electron group. This threshold is selected such that only the fast electrons are capable of inelastic processes. In the single-beam model, the threshold is set at the ionization energy.[7] In the multibeam model, the threshold is the excitation energy.

In the single-beam model, all fast electrons are assumed to have the same velocity at any given position. This implies that the energy distribution function is a δ function. Thus, all that is needed to characterize fast electrons are number density n_{be} and velocity u_{be}. Only two equations are required to solve for these quantities.[6,21] The usual approach is to use species conservation

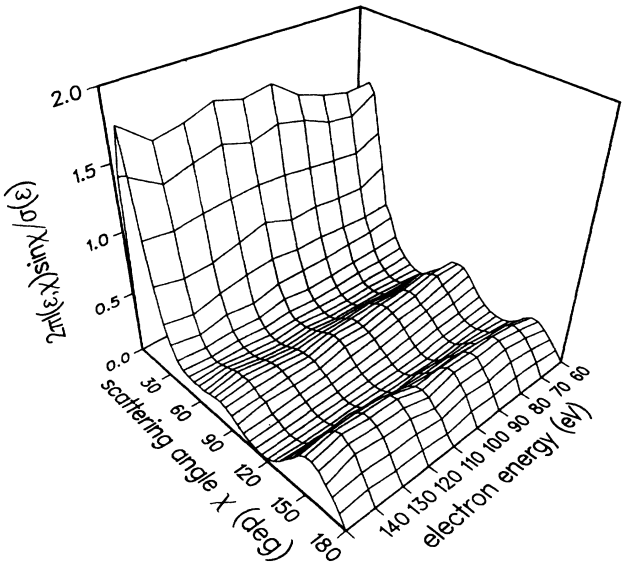

FIG. 2. Normalized differential cross sections for elastic scattering in argon from Vuskovic and Kurepa (Ref. 30). We have extrapolated their data (5°–150°) to cover the entire range of scattering angles (0°–180°).

and energy (as opposed to momentum) conservation. The single-beam model that we use is from Boeuf and Segur,[8]

$$\frac{dj_{be}}{dx}=(1-\alpha)r_i \quad \text{for } \varepsilon_{be}>\varepsilon_{\text{ion}} \tag{7a}$$

and

$$\frac{dj_{be}}{dx}=-\alpha r_d \quad \text{for } \varepsilon_{be}\le\varepsilon_{\text{ion}} , \tag{7b}$$

where

$$r_i=\sigma_{\text{ion}}(\varepsilon_{be})u_{be}n_n n_{be} \tag{8a}$$

and

$$r_d=\sigma_{\text{en}}u_{be}n_n n_{be} . \tag{8b}$$

Equations (7a) and (7b) are the species conservation equations for fast electrons above and below the ionization threshold ε_{ion}, respectively. r_i is ionization rate and $\sigma_{\text{ion}}(\varepsilon_{be})$ is the ionization cross section. In the single-beam model, beam growth occurs only in the cathode fall, hence α is 0 in the cathode fall and 1 in the negative glow. When the energy of the fast electrons ($\varepsilon_{be}=m_e u_{be}^2/2$) drops below ε_{ion}, fast electrons are lost to the slow group at a rate r_d. This rate is based on an approximate total collision cross section $\sigma_{\text{en}}(\sim 10^{-15}\ \text{cm}^2)$. Thus C_+ is r_i, whereas C_e [Eq. (1)] is αr_i when $\varepsilon_{be}>\varepsilon_{\text{ion}}$, and is αr_d when $\varepsilon_{be}\le\varepsilon_{\text{ion}}$. The form for r_d is based on the idea that below the ionization energy, electrons drop from the fast group into the slow group through momentum-transfer collisions. This is clearly a crude approximation, but in the framework of the single-beam model, the *ad hoc* nature of this assumption is probably inevitable.

The corresponding fast-electron energy-conservation equations are

$$\frac{dj_{be}\varepsilon_{be}}{dx}=ej_{be}\frac{dV}{dx}-(r_i\varepsilon_{\text{ion}}+r_e\varepsilon_{\text{ext}}) \quad \text{for } \varepsilon_{be}>\varepsilon_{\text{ion}} \tag{9a}$$

and

$$\frac{dj_{be}\varepsilon_{be}}{dx}=ej_{be}\frac{dV}{dx}-(r_d\varepsilon_{be}+r_e\varepsilon_{\text{ext}}) \quad \text{for } \varepsilon_{be}\le\varepsilon_{\text{ion}} \tag{9b}$$

where

$$r_e=\sigma_{\text{ext}}(\varepsilon_{be})u_{be}n_n n_{be} . \tag{10}$$

r_e is the total excitation rate and $\sigma_{\text{ext}}(\varepsilon_{be})$ is the total excitation cross section. Substituting Eq. (7) into Eq. (9) allows us to eliminate j_{be} since $j_{be}=u_{be}n_{be}$:

$$\frac{d\varepsilon_{be}}{dx}=e\frac{dV}{dx}-[\sigma_{\text{ion}}(\varepsilon_{be})n_n\varepsilon_{\text{ion}}+\sigma_{\text{ext}}(\varepsilon_{be})n_n\varepsilon_{\text{ext}}] -(1-\alpha)\sigma_{\text{ion}}(\varepsilon_{be})n_n\varepsilon_{be} \quad \text{for } \varepsilon_{be}>\varepsilon_{\text{ion}} \tag{11a}$$

and

$$\frac{d\varepsilon_{be}}{dx}=e\frac{dV}{dx}-\sigma_{\text{ext}}(\varepsilon_{be})n_n\varepsilon_{\text{ext}} \quad \text{for } \varepsilon_{be}\le\varepsilon_{\text{ion}} . \tag{11b}$$

Equations (7) and (11) are integrated over a discrete grid from the cathode to obtain j_{be} and ε_{be}. The boundary conditions at the cathode are $j_{be}=-\gamma j_+$ [Eq. (6)] and $\varepsilon_{be}=1$ eV.

In the multibeam model, the assumption that all fast electrons have the same velocity at any position is relaxed. However, all fast electrons are still assumed to be purely forward directed. The method that we use is an adaptation of the model which is described in detail by Carman and Maitland.[23] This technique is comparable to a Monte Carlo simulation with completely forward scattered fast electrons. Comparisons made by Carman and Maitland[23] to the Monte Carlo simulation of a helium cathode fall by Tran, Marode, and Johnson support this assertion. We have made similar comparisons (Sec. V), the results of which demonstrate that the two approaches are indeed closely related. In Appendix A we discuss the relationship of the multibeam model to the Boltzmann equation with the assumption of full forward scattering.

In this model, the fast-electron flux energy distribution $J_{be}(x,\varepsilon)$ is tracked from the cathode to the anode. The fast electron flux is given by

$$j_{be}(x)=\int_0^\infty J_{be}(x,\varepsilon)d\varepsilon . \tag{12a}$$

$J_{be}(x,\varepsilon)$ is discretized over energy space in $\Delta\varepsilon$ intervals. Thus the integral in Eq. (12a) is replaced with a sum,

$$j_{be}(x)=\sum_{\varepsilon_k=0}^{\infty} J_{be}(x,\varepsilon_k)\Delta\varepsilon . \tag{12b}$$

Setting $\Delta\varepsilon$ equal to 1 eV is convenient since the ionization threshold (16 eV) and excitation threshold (12 eV) are then exact multiples of $\Delta\varepsilon$.

Since all fast electrons are assumed forward directed, the distance they travel from x_i to $x_i+\Delta x_i$ is Δx_i. The energy change that fast electrons undergo is dependent on the change in potential energy ΔeV_i, and the possibility of inelastic collisions. The fraction of fast electrons in a bin at energy ε_k that make an inelastic collision after traveling a distance Δx_i is given by

$$\Delta J_{be}(x_i,\varepsilon_k)=J_{be}(x_i,\varepsilon_k)\{1-\exp[-\Delta x_i/\lambda_{\text{in}}(\varepsilon_k)]\} , \tag{13}$$

where the inelastic mean free path $\lambda_{\text{in}}(\varepsilon_k)$ is given by

$$\lambda_{\text{in}}(\varepsilon_k)=\frac{1}{[\sigma_{\text{ion}}(\varepsilon_k)+\sigma_{\text{ext}}(\varepsilon_k)]n_n} . \tag{14}$$

The fraction that does make a collision is split into an ionization part, $\Delta J_{be,\text{ion}}(x_i,\varepsilon_k)$, and an excitation part, $\Delta J_{be,\text{ext}}(x_i,\varepsilon_k)$, in the ratio $\sigma_{\text{ion}}:\sigma_{\text{ext}}$. Since slow electrons are not created in the cathode fall, the fraction of fast electrons that are created, $\Delta J_{be,\text{new}}(x_i,\varepsilon_k)$, is equal to $\Delta J_{be,\text{ion}}(x_i,\varepsilon_k)$. The excitation fraction is transferred to the bin at $(x_i+\Delta x_i,\varepsilon_k-\varepsilon_{\text{ext}}+\Delta eV_i)$. Ionization is more complicated because the progeny (or ejected) electron can be created at any energy p, ranging from 0 to $(\varepsilon_k-\varepsilon_{\text{ion}})/2$. $\sigma_{\text{ion}}(\varepsilon)$ is related to the ionization cross section distribution $S(\varepsilon,p)$ by

$$\sigma_{\text{ion}}(\varepsilon_k)=\int_0^{(\varepsilon_k-\varepsilon_{\text{ion}})/2} S(\varepsilon_k,p)dp . \tag{15a}$$

For the purposes of the discrete model, the integral in Eq.

(15a) is replaced with a sum,

$$\sigma_{\text{ion}}(\varepsilon_k)=\sum_{p_j=1}^{p_{\max}} S(\varepsilon_k,p_j)\Delta p$$

$$\text{where } p_{\max}=\text{int}\left[\frac{\varepsilon_k-\varepsilon_{\text{ion}}}{2}\right]. \quad (15b)$$

Δp is chosen to be equal to $\Delta\varepsilon$, i.e., $\Delta p=\Delta\varepsilon=1$ eV. In Eq. (15b) the minimum energy of the progeny electron is set at 1 and not 0 eV, so as to avoid a nonzero flux bin at 0 eV. The density of fast electrons in the 0-eV bin will be infinite if $J_{be}(x,0)$ is not zero. Hence the lowest energy at which a fast electron is capable of an ionizing collision in this model is 18 eV. Similarly, only fast electrons with energies of 13 eV or greater can excite neutral molecules.

The distribution of the new fast-electron flux is based on $S(\varepsilon_k,p_j)$ for $1\le p_j\le \text{int}[(\varepsilon_k-\varepsilon_{\text{ion}})/2]$. The contribution of $\Delta J_{be,\text{new}}(x_i,\varepsilon_k)$ to a bin at $(x_i+\Delta x_i,p_j+\Delta eV_i)$ is $\Delta J_{be,\text{new}}(x_i,\varepsilon_k)[S(\varepsilon_k,p_j)/\sigma_{\text{ion}}(\varepsilon_k)]$. Correspondingly, the contribution of $\Delta J_{be,\text{ion}}(x_i,\varepsilon_k)$ to the bin at $(x_i+\Delta x_i,\varepsilon_k-\varepsilon_{\text{ion}}-p_j+\Delta eV_i)$ is $\Delta J_{be,\text{ion}}(x_i,\varepsilon_k)[S(\varepsilon_k,p_j)/\sigma_{\text{ion}}(\varepsilon_k)]$. Δx_i is chosen such that ΔeV_i is an exact multiple of $\Delta\varepsilon$. Because ε_{ion} (16 eV), ε_{ext} (12 eV), Δp (1 eV), and ΔeV_i are exact multiples of $\Delta\varepsilon$ (1 eV), the following expression can be used to calculate the flux distribution of the fast electrons at any point in the cathode fall:

$$\begin{aligned}J_{be}(x_i+\Delta x_i,\varepsilon_k+\Delta eV_i)=&J_{be}(x_i,\varepsilon_k)-\Delta J_{be}(x_i,\varepsilon_k)+\Delta J_{be,\text{ext}}(x_i,\varepsilon_k+\varepsilon_{\text{ext}})\\&+\sum_{\varepsilon_n=0}^{\infty}\Delta J_{be,\text{ion}}(x_i,2\varepsilon_k+\varepsilon_{\text{ion}}+\varepsilon_n)\frac{S(2\varepsilon_k+\varepsilon_{\text{ion}}+\varepsilon_n,\varepsilon_k)}{\sigma_{\text{ion}}(2\varepsilon_k+\varepsilon_{\text{ion}}+\varepsilon_n)}\\&+\sum_{p_j=1}^{\varepsilon_k}\Delta J_{be,\text{ion}}(x_i,\varepsilon_k+\varepsilon_{\text{ion}}+p_j)\frac{S(\varepsilon_k+\varepsilon_{\text{ion}}+p_j,p_j)}{\sigma_{\text{ion}}(\varepsilon_k+\varepsilon_{\text{ion}}+p_j)}.\end{aligned} \quad (16)$$

In Eq. (16), the second term on the right is the fraction that is lost from the energy bin. The third and fourth terms are the fraction of electrons that enter the bin after an excitation and ionization collision, respectively. The last term accounts for the electrons that are created at the bin energy.

The situation in the negative glow, however, is more complicated. First, the fast-electron flux in the bins with ε_k less than or equal to ε_{ext} ($\varepsilon_k\le 12$ eV) are lost to the slow group at a collisional rate corresponding to σ_{en} ($\sim 10^{-15}$ cm^{-2}). The fraction of the flux lost in a distance Δx_i in this manner $\Delta J_{be,\text{en}}(x_i,\varepsilon_k)$, is also given by Eq. (13), with λ_{en} replacing λ_{in}, where $\lambda_{\text{en}}=1/\sigma_{\text{en}}n_n$. Second, progeny electrons that are created with energies less than or equal to ε_{ext} ($p_j\le 12$ eV) are put in the slow-electron group. Thus fast-electron creation can continue to occur in the negative glow, whereas in the single-beam model all ionization in the negative glow results in slow-electron formation. Third, the fraction of the fast electrons that have resultant energies less than or equal to ε_{ext} after an inelastic collision also enter the slow group. In Appendix B we present the details of calculating the creation rates C_e and C_+.

Some care is required in keeping track of the fast-electron flux and the various creation rates, otherwise problems with charge conservation can occur. The appropriate boundary condition at the cathode is $J_{be}(0,1)=-\gamma j_+$ and $J_{be}(x,k)=0$ for $k\neq 1$.

D. Numerical simulation

The numerical simulation consists of the fast-electron model (either single-beam or multibeam) combined with the fluid model. The solution technique is an iterative procedure. The flowchart for this scheme is shown in

Fig. 3. The initial guess for the electric field and the fast-electron flux at the cathode is usually obtained from a previous solution, or from a suitably contrived representation of some experimental data. In the latter case, the potential drop across the discharge V_c, approximate cathode-fall thickness d_c, and current density j, are re-

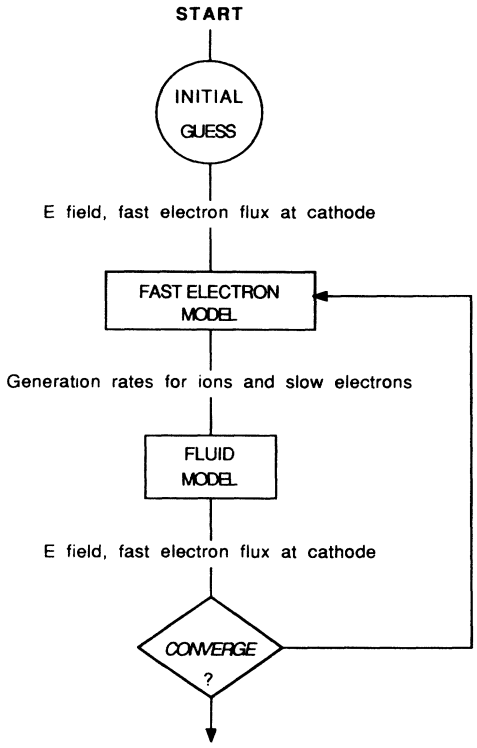

FIG. 3. Flowchart of solution technique.

quired. The following equations can then be used for a linearly decreasing field E, in the cathode fall and zero field in the rest of the region:

$$E=-\frac{2V_c}{d_c}\left[1-\frac{x}{d_c}\right] \quad \text{for } 0\le x\le d_c \tag{17}$$

and

$$j_{be,\text{cathode}}=-\frac{j\gamma}{1+\gamma} . \tag{18}$$

As discussed in the previous section, the creation rates of ions and slow electrons are calculated in the fast-electron models. These rates are used as inputs to the fluid model. The solution of the governing equations in the fluid model with these creation rates gives rise to a new electric field profile and ion flux at the cathode. The new information is used in the fast-electron models to recalculate the creation rates. This procedure is repeated until convergence is obtained. Typically, the difference between the solution at convergence and the previous solution from either beam model is less than 0.1%.

In the simulation of fast electrons, it is necessary to distinguish between the negative-glow and cathode-fall regions. We have used a cutoff based on the potential to separate the two regions. We found it convenient to use $V=0$ (i.e., $V<0$ in the cathode fall and $V\ge 0$ in the negative glow) in our simulations. The results of our examination of the sensitivity of the solutions to the cutoff are presented below. Other candidates for the cutoff can be based on the electric field,[8,20] or space-charge density.

The fluid model was solved using the Galerkin finite-element method. The resulting system of equations was integrated through time until steady state was achieved. The spatial grid was nonuniform, with the highest density of nodes in the cathode fall and at the negative-glow–cathode-fall boundary.

E. Cross sections and transport parameters

The cross sections for argon are shown in Fig. 4. The composite excitation cross section is from Eggarter.[32] The ionization cross-section distribution is from Peterson and Allen.[33] This distribution was integrated as in Eq. (15) and the result is shown. The elastic cross section is from a fit to the data in Hayashi.[34]

Differential cross sections are required for the particle simulations described in the next section. Due to the relative scarcity of data, we use an analytic expression based on its look-alike, screened Coulomb scattering,[35]

$$f(\varepsilon,\chi)=\frac{\varepsilon}{4\pi[1+\varepsilon\sin^2(\chi/2)]\ln(1+\varepsilon)} , \tag{19}$$

where $f(\varepsilon,\chi)=I(\varepsilon,\chi)/\sigma(\varepsilon)$ (Fig. 5). By choosing such a formulation, we keep the total cross section constant while varying the nature of angular scattering.[5] This expression captures the main features of electron-neutral scattering: it is approximately isotropic $[f(\varepsilon,\chi)=1/4\pi]$ at low energies and becomes increasingly anisotropic as the energy increases. It is of interest to note that the ratio of the momentum cross section $\sigma_m(\varepsilon)$, to the total cross section $\sigma(\varepsilon)$, which is given by

$$\frac{\sigma_m(\varepsilon)}{\sigma(\varepsilon)}=\int_0^{\pi}2\pi(1-\cos\chi)(\sin\chi)f(\varepsilon,\chi)d\chi$$
$$=\frac{2}{\ln(1+\varepsilon)}\left[1-\frac{\ln(1+\varepsilon)}{\varepsilon}\right] , \tag{20}$$

decreases monotonically with energy. In the isotropic limit ($\varepsilon\to 0$ eV), this ratio is 1, but it drops to 0.63 at $\varepsilon=10$ eV and to 0.41 at $\varepsilon=100$ eV. This is an important consideration because $\sigma_m(\varepsilon)$ and not $\sigma(\varepsilon)$ is kept constant in Boltzmann calculations that treat anisotropic scattering.[36]

Furthermore, it should be noted that Eq. (19) does not contain the complex structure of the differential cross sections in Ar at very low energies.[31] Nonetheless, this choice of $f(\varepsilon,\chi)$ is convenient since the scattering angle χ can be easily determined with a uniformly distributed random number R_i $(0\le R_i\le 1)$,

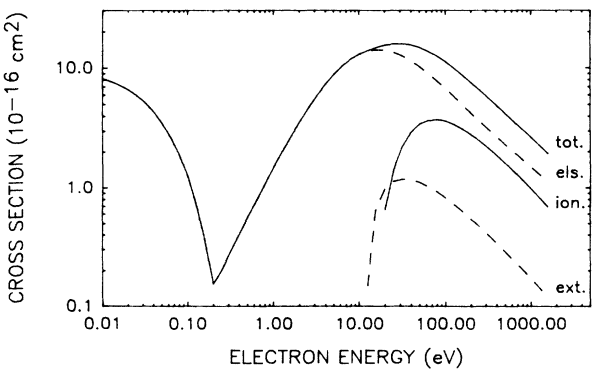

FIG. 4. Cross sections (total, elastic, ionization, composite excitation) for electron-neutral collisions in argon.

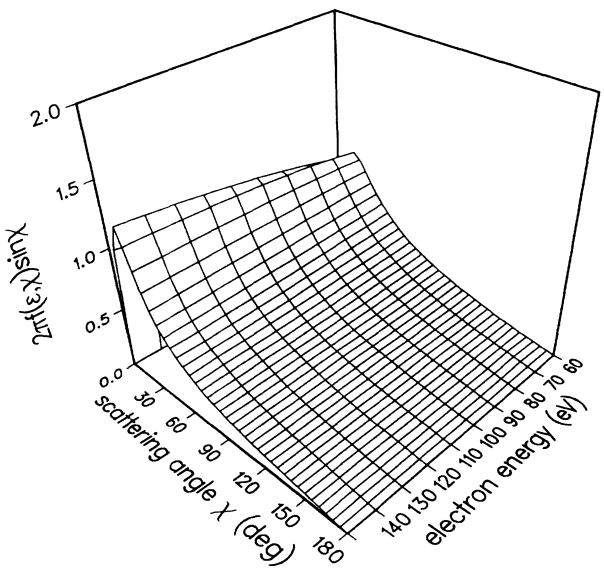

FIG. 5. Normalized differential cross sections used in particle simulations.

$$R_i = \int_0^{\chi} 2\pi f(\varepsilon,\chi')\sin\chi' d\chi' \ . \tag{21}$$

Data in Massey and Burhop[31] suggest that inelastic scattering is approximately similar to elastic scattering of an electron with energy equivalent to the energy of an electron after the inelastic collision (e.g., the progeny electron from an ionizing collision involving a 100-eV electron will scatter much more anisotropically if it is ejected with an energy of 42 eV as opposed to 1 eV). We thus use Eq. (19) for all collisions, with ε being the electron energy after the collision.

The electron transport parameters at 1 torr are as follows: $D_e = 2\times10^5$ cm^2 s^{-1} and $\mu_e = 2\times10^5$ cm^2 V^{-1} s^{-1}. The ion diffusivity at 1 torr that we used is an artificially high value of 400 cm^2 s^{-1}. This high value helped reduce wiggles, if any, in the ion density profile at the cathode-fall–negative-glow boundary. It did not have any other noticeable impact on the solutions, since the contribution of diffusion to the overall ion transport is minimal. The ion mobility[37] is in the form of a fit suggested by Frost:[38]

$$\mu_+ = \mu_{+0}(1+a|E/n_n|)^{-1/2} \ , \tag{22}$$

where a is 7.36×10^{14} cm^{-2} V^{-1}, and μ_{+0} at 1 torr is 1420 cm^2 V^{-1} s^{-1}.

The value of γ was set at 0.033 in the single-beam model and 0.07 in the multibeam model.

F. Particle simulations

Various Monte Carlo methods have been used to simulate the electron avalanche in the cathode region of dc discharges.[5,16,18,39] Most of these utilize the null-collision method,[16,40] which is accurate and computationally efficient. The technique that we use is based on particle tracking methods that are used in particle simulations.[41] Despite being computationally more intensive than the null-collision method, this technique can be readily incorporated into dynamic simulations of plasmas.[42]

In this technique, the positions and velocities of particles are calculated every time step Δt. The collision probability q_m is given by

$$q_m = 1-\exp\left[\frac{-\Delta s_m}{\lambda(\varepsilon_m)}\right] , \tag{23}$$

where Δs_m is the distance the mth particle travels in Δt, and $\lambda(\varepsilon_m)$ is the total mean free path [$1/\sigma_{\rm tot}(\varepsilon)n_n$, $\sigma_{\rm tot}(\varepsilon)$ is from Fig. 4]. This imposes constraints on Δt, as ε_m should not change significantly in each time step, and $\Delta s_m/\lambda(\varepsilon_m)$ should not be much larger than 0.1. A collision takes place if a uniformly distributed random number on the interval [0,1] is less than q_m. If a collision does take place, more random numbers are used to determine the nature of the collision, the energy of the progeny electron (for an ionization collision), and the new direction(s). The procedure for this is described in detail by Boeuf and Marode.[16]

We consider three different scattering assumptions: isotropic scattering, anisotropic scattering, and full forward scattering. In isotropic scattering the differential cross section $I(\varepsilon,\chi)$ is constant over all χ, whereas we use Eq. (19) for all collisions in the anisotropic scattering case. As noted in the previous section, the electron energy immediately after the collision is used in calculating the scattering angle. The full forward scattering case provides a comparison to the multibeam model.

Particles are injected into the discharge from the cathode with an energy of 1 eV and zero transverse velocity at a rate proportional to the secondary electron emission flux [Eq. (6)]. The electrodes are assumed to be perfectly absorbing.

Once the particles enter the negative glow, only fast electrons are tracked. As in the multibeam model, particles that are on the anode side of the cutoff with energies less than $\varepsilon_{\rm ext}$ are transferred to the slow-electron group. This is done at every time step in the particle simulation. In this manner we avoid the enormous cost of tracking the large number of particles that would accumulate in the negative glow. The particles are weighted to the grid using standard particle-in-cell techniques.[41] Relevant quantities such as ion and slow-electron creation rates are obtained by averaging over many time steps after the simulation reaches steady state. We use the method described in Sec. II D to obtain self-consistent results (i.e., the creation rates are fed back into the fluid model to recalculate the electric field and boundary conditions, and the process is repeated until convergence is obtained). It should be noted that due to the stochastic nature of the particle simulation, convergence and charge conservation issues are more critical than in the beam models.

We have checked our particle simulations by calculating swarm parameters for constant E/n_n. Our results are in reasonable agreement with those of Sakai, Tagashira, and Sakamoto.[43]

III. SINGLE-BEAM MODEL RESULTS

The first set of results (Fig. 6) is for the single-beam model. They are similar to those obtained by other researchers who used the single-beam model.[8,20] The plot of the species densities [Fig. 6(a)] together with electric field and potential profiles [Fig. 6(b)] indicate that the sheath edge is about 2.2 mm from the cathode. The ion density in the cathode fall is almost constant. This gives rise to an electric field that drops approximately linearly from about 1500 V/cm to a small value at the sheath edge, and remains small beyond this point. The voltage at this point is also about 0 V, which indicates that our assumption about the location of the sheath edge in the numerical simulation (Sec. II D) is consistent. Both electron and ion densities rise rapidly beyond this point and become very nearly equal in magnitude.

The ionization rate peaks at the sheath edge, while the excitation rate peaks farther into the low-field region [Fig. 6(c)]. The difference in the shapes of these profiles is due to the differences between the ionization and excitation cross sections (Fig. 4). While both cross sections vary as $\varepsilon^{-1}\ln\varepsilon$ at high energies,[32] $\sigma_{\rm ext}(\varepsilon)$ peaks sooner and more sharply than $\sigma_{\rm ion}(\varepsilon)$. Thus in the context of the single-beam model, it is possible to find cases in which inelastic rates increase as beam energy decreases (this situation is discussed in the next section).

Figure 6(d) demonstrates how the current is carried in the discharge. The total current is a sum of the three fluxes,

$$ej = e[j_+(x) - j_{be}(x) - j_e(x)] \ . \tag{24}$$

The assumptions in the single-beam model force the slow-electron flux to zero in the cathode fall, and the fast-electron flux to be constant beyond the point at which $j_e(x)$ starts to grow. The discontinuity in j_e at about 7 mm is due to the fact that ε_{be} is below ε_{ion}, causing the fast electrons to drop in to the slow-electron group [Eq. (7b)].

Ions are the major charge carriers to the cathode, whereas the slow electrons carry most of the current to the anode. Note, however, that there is a nonzero ion flux to the anode as well. There is a field reversal at 5.30 mm, where j_+ goes through zero (ion transport is almost completely dominated by field-induced drift). This happens slightly to the anode side of the maximum in the species densities, which is at 5.37 mm. Thus the ion flux on the cathode side of the field reversal is directed towards the cathode, and on the anode side to the anode.

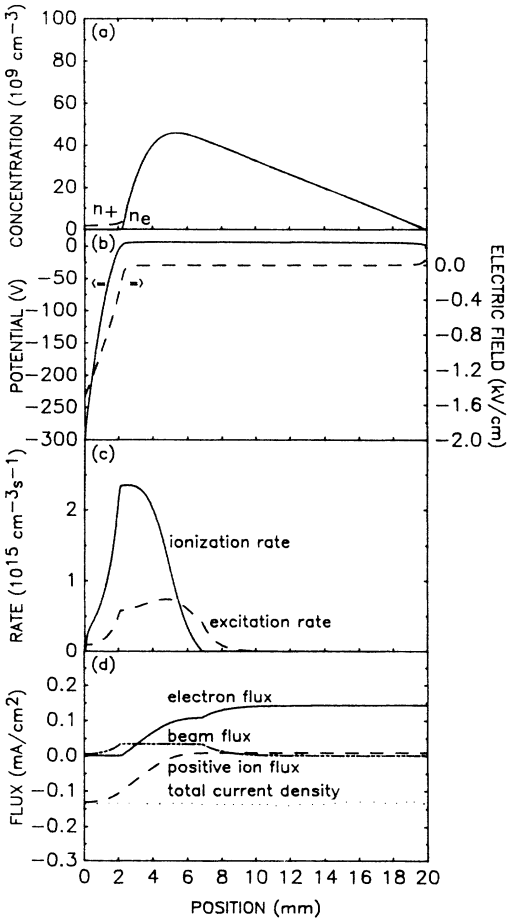

FIG. 6. Solution to the single-beam model (300 V, 0.6 torr): (a) slow-electron and ion densities; (b) potential and electric field; (c) inelastic rates; (d) charged particle fluxes and total current density. The field reversal occurs at 5.37 mm and the species density maximum is at 5.30 mm.

IV. MULTIBEAM MODEL RESULTS

Although results from the single-beam model are usually qualitatively correct, a number of discrepancies are apparent on comparison to results from the multibeam model under similar conditions. As discussed in Sec. II D, a cutoff that distinguishes the low-field region from the high-field region is required. The position of this cutoff should not significantly influence the results, since the choice is arbitrary. In Fig. 7 we show the sensitivity of both models to the position of the cutoff. In the case of our single-beam model [Fig. 7(a)], the ionization rate profile is lower but extends farther into the discharge when the cutoff is changed from -10 to 0 V. The lower ionization rate is due to the fact that fast-electron flux growth is stopped closer to the cathode [Eq. (7a)]. However, beam energy is higher at the cutoff [Eq. (11a)], hence the beam extends farther into the discharge. This difference in ionization rate profile causes a disturbingly large change in discharge current (from 0.140 mA/cm^2 to 0.158 mA/cm^2 when the cutoff is moved from -10 to 0 V). The multibeam model, however, is much less sensitive to the same change in cutoff. The difference in ionization rate is imperceptible in Fig. 7(b), and the discharge current changes only from 0.119 mA/cm^2 to 0.120 mA/cm^2 when the cutoff is moved from -10 to 0

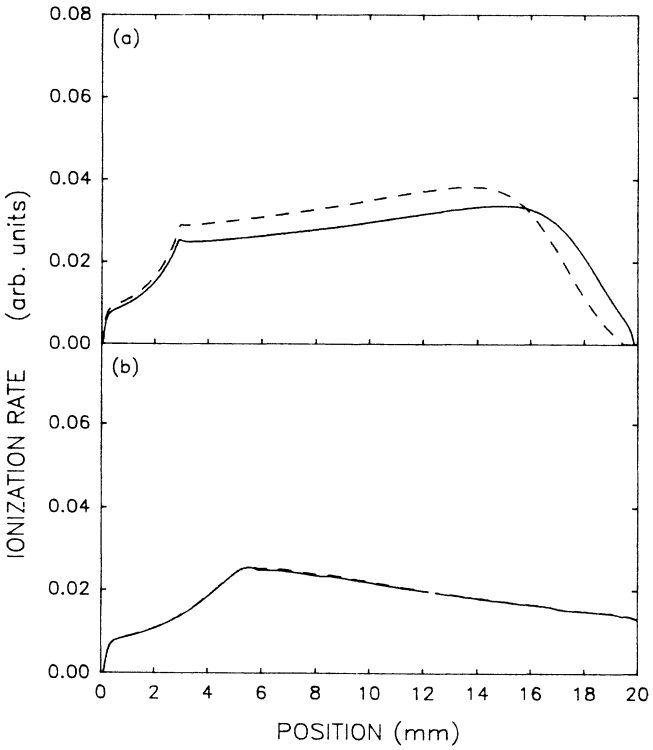

FIG. 7. Effect of cutoff on solutions to (a) single-beam and (b) multibeam models. Solid line, cutoff at -10 V; dashed line, cutoff at 0 V. In the single-beam model, changing the cutoff from -10 to 0 V changes the current density from 0.140 to 0.158 mA/cm^2, whereas in the multibeam model, the current density changes only from 0.119 to 0.120 mA/cm^2. Conditions are 500 V and 0.6 torr.

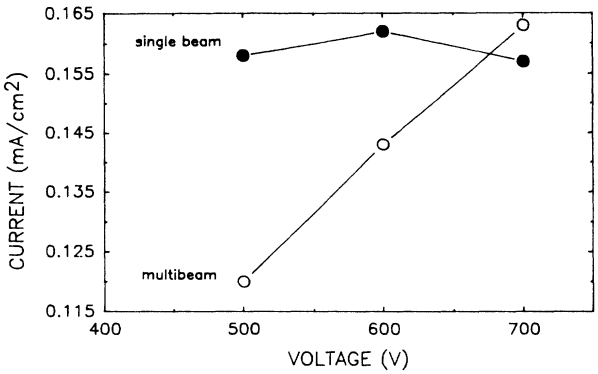

FIG. 8. Comparison of I-V characteristics at 0.4 torr from single-beam and multibeam models.

V. In the multibeam model, additional electrons that would be treated as fast electrons by moving the cutoff are at the low end of the energy spectrum, and do not influence the ionization rate. Clearly, the extra effort in calculating a distribution of electron energy with the multibeam model pays off in a more accurate simulation as compared to the single-beam model.

The other difference between the single-beam and multibeam models is the disparate behavior of the voltage-current characteristics under certain conditions. As shown in Fig. 8, the single-beam model predicts a negative voltage-current characteristic, whereas the multibeam model does not. It should be noted that while negative voltage-current characteristics are not necessarily unphysical, our results indicate that the single-beam model has a greater propensity to predict negative characteristics than the multibeam model. (We have never observed negative characteristics with the multibeam model under the range of conditions that we have investigated: 0.4 to 2 torr, 200 to 700 V, 2-cm electrode gap.) We note that the single-beam model tends to predict negative characteristics in cases with high voltages and low pressures (Fig. 8), where the beam can traverse the entire discharge. This is not surprising, considering σ_{ion} varies as $\varepsilon^{-1}\ln\varepsilon$ at high energies, and the assumption of a monoenergetic beam. From Eq. (8a), for a constant beam flux and a relatively high energy beam, a rise in energy can result in a drop in the ionization rate. This effect is diminished in the multibeam model because the creation of energetic progeny electrons (Sec. II C) is a very effective method of spreading out the energy distribution of fast electrons.

In Fig. 9 we present the energy distribution of the fast-electron flux $J_{be}(x,\varepsilon)$ at various positions in the cathode fall (the conditions are the same as in Fig. 6). The most salient feature of this figure is the wide spread of energies in the distribution. The distribution cannot be adequately described by a monoenergetic beam. The peak at the highest energy is the electrons that have not suffered any inelastic collisions, and the next peak is the electrons that have suffered one excitation collision. Below this peak is a distribution of electrons, which is the result of creating energetic progeny electrons. From Fig. 9 it is clear that

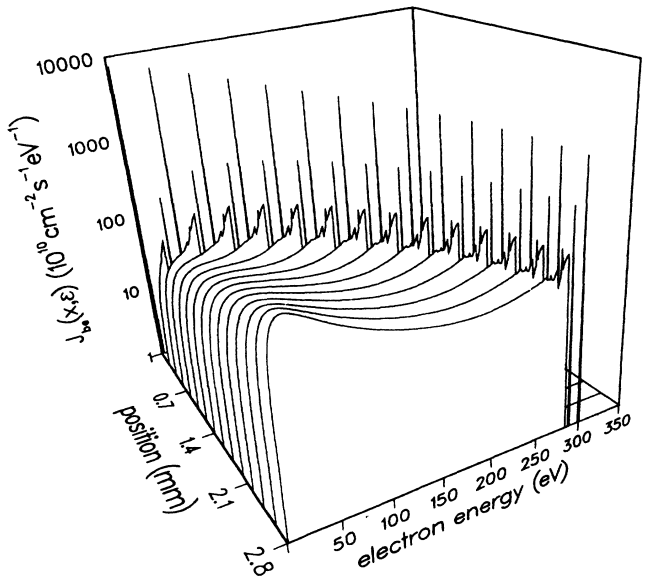

FIG. 9. Energy distribution of the fast-electron flux $J_{be}(x,\varepsilon)$. Conditions are 300 V and 0.6 torr.

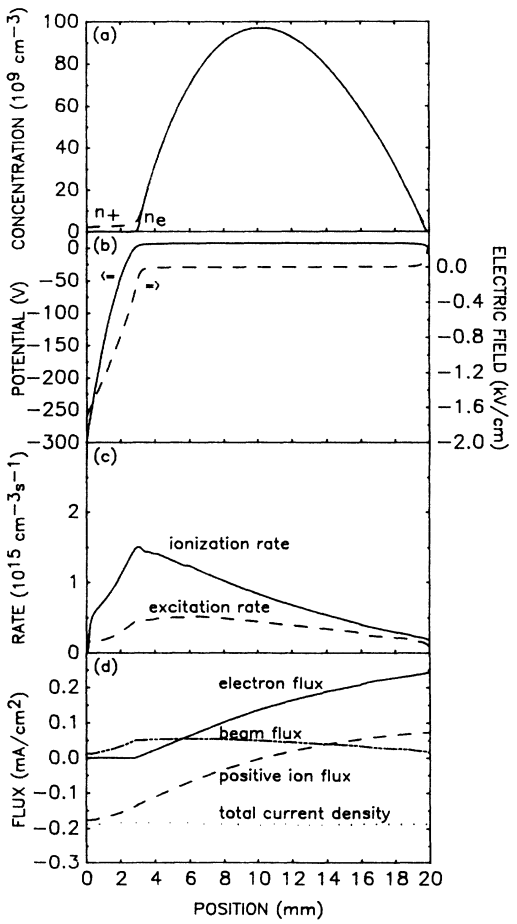

FIG. 10. Solution to the multibeam model: (a) slow-electron and ion densities; (b) potential and electric field; (c) inelastic rates; (d) charged particle fluxes and total current density. The conditions are the same as in Fig. 9 (300 V, 0.6 torr). The field reversal occurs at 10.22 mm and the species density maximum is at 10.14 mm.

under these conditions, a substantial fraction of electrons emitted from the cathode have not undergone any inelastic collisions by the time they reach the sheath edge.

Figure 10 shows the results from the multibeam model. It is the equivalent of Fig. 6. The inelastic rates extend much farther into the discharge [Fig. 10(c)] than in the single-beam case [Fig. 6(c)]. Correspondingly, the species density profiles [Fig. 10(a)] are more symmetric, and the ion flux to the anode is larger [Fig. 10(d)]. This is the direct result of not having averaged away the high-energy tail as in the single-beam model.

The field reversal (at 10.22 mm) is again just slightly to the anode side of the maximum in species densities (at 10.14 mm). The presence of field reversals has been demonstrated in measurements and single-beam model predictions by Gottscho *et al.*[20] (in Ar/N_2 discharges). Their results indicate that field reversals can occur on either side of the maximum in species densities. It should be noted that our current description of the slow-electron transport with constant parameters is not adequate to accurately predict the location of field reversals. From Eq. (4), a field reversal on the cathode side of the species density maximum would imply that j_e is negative (i.e., directed towards the cathode) in the region between the field reversal and the species density maximum. Since j_e is zero in the cathode fall, a negative j_e requires that dj_e/dx be negative in some region. This can only happen if there is some form of loss mechanism for slow electrons [Eq. (1), with $\partial n_e/\partial t = 0$ for steady state], which we have not included. A more accurate treatment of the slow-electron transport would require a generalization of Eq. (4) with energy-dependent transport parameters and an energy balance for the slow electrons.

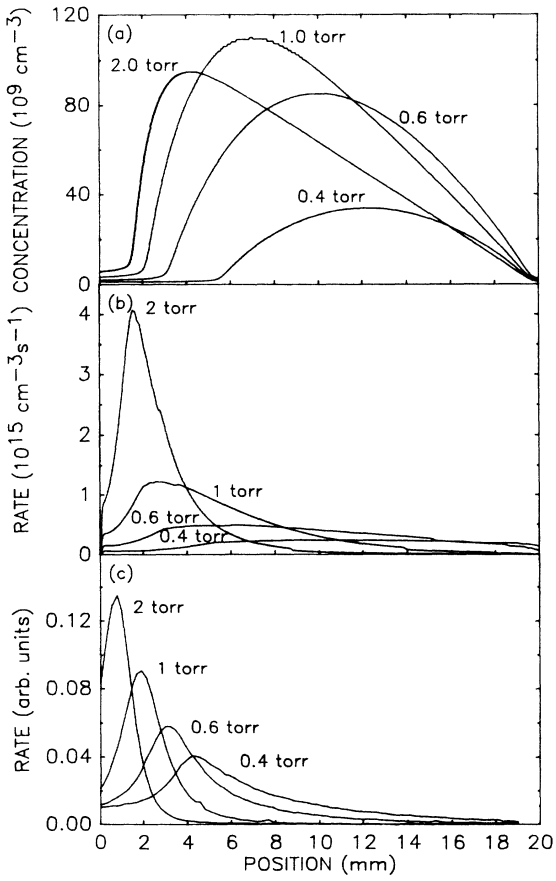

FIG. 11. Results at a constant power density of 0.05 W/cm^2: (a) ion density profiles from the multibeam model; (b) excitation rate profiles from the multibeam model; (c) experimental optical-emission (419.832 nm; $1s_4$-$3p_5$ in Paschen notation) profiles.

In Fig. 11 we present the predictions of the multibeam model at constant power and a comparison to experimental measurements. The results indicate that the species density profiles [Fig. 11(a)] become more asymmetric, and the inelastic rates [Fig. 11(b)] become more peaked at the cathode sheath edge as the pressure increases. The trend in the excitation rate is consistent with our emission measurements [Fig. 11(c)] and other emission measurements in similar systems.[44] However, the model predictions of the excitation rate extend much farther into the discharge than the emission measurements. This is a direct consequence of the assumption of full forward scattering in the multibeam model. The fast electrons penetrate far into the discharge because they do not scatter off axis. Nonetheless, the multibeam model is a qualitatively accurate representation of the discharge over a wide range of conditions.

V. PARTICLE SIMULATIONS

A. Swarm simulation of fast electrons

In this section we discuss results from Monte Carlo simulations of fast electrons that originate at the cathode and progeny electrons that result from ionizing collisions in the sheath. The use of a Monte Carlo simulation for fast electrons allows us to examine the effects of various scattering assumptions: isotropic, anisotropic, and pure forward scattering on the discharge structure. The results presented in Figs. 12 and 13 use the electric field profile and secondary electron flux at the cathode from the multibeam calculations at 0.6 torr and 275 V. Hence these results are not self-consistent, unlike the results in the previous sections. Nonetheless, they are useful in examining the importance of angular scattering of fast electrons in collisions with neutrals. Preliminary self-consistent hybrid particle-fluid calculations are discussed in the next section.

In Fig. 12 we present a snapshot of the energy and position of the particles at one instant in time. Only approximately 1000 particles from each simulation are shown. Note that in the low-field region (>3 mm) only particles with energy greater than ε_{ext} are tracked. The particles that enter this region of phase space ($x > 3$ mm, $\varepsilon < \varepsilon_{ext}$) are shifted into the slow-electron group at each time step (there are a few particles visible in this region in Fig. 12 because the snapshot was taken before the particles were shifted). With isotropic scattering [Fig. 12(a)], fast electrons are highly concentrated around the plasma sheath edge. These electrons penetrate a little farther into the discharge with anisotropic scattering [Fig. 12(b)],

whereas they are almost evenly distributed throughout the discharge with forward scattering [Fig. 12(c)]. The reason for this is clear: angular scattering causes fast electrons to spend a significantly greater amount of time near the cathode.

In Fig. 13 the inelastic rates corresponding to these cases [Figs. 13(a)–13(c)] are plotted together with results from the multibeam model [Fig. 13(d)], and emission measurements [Fig. 13(e)] under the same conditions. Figures 13(a) and 13(b) indicate that inelastic rate profiles are strongly peaked at the cathode sheath edge with angular scattering (anisotropic scattering causes the profiles to extend farther into the discharge than isotropic scattering). These profiles are similar to those obtained by Den Hartog, Doughty, and Lawler[5] and Moratz.[39] The major difference between the two cases is that the rates are almost a factor of 3 higher with isotropic scattering. This is because fast electrons are more localized near the cathode with isotropic scattering. Boeuf and Marode[16] observed little difference in their results (He discharge: 1 torr, 150 V, 1.5 cm electrode gap) when they substituted anisotropic with isotropic scattering for elastic collisions. However, they used isotropic scattering for excitation collisions and an *ad hoc* anisotropic scattering scheme for ionization collisions. In this scheme they assume that (i) incident, scattered, and ejected electrons are coplanar; and (ii), scattered and ejected electron velocities are perpendicular. Furthermore, it is unclear as to whether they maintained a constant total cross section or momentum-transfer cross section when they switched from isotropic to anisotropic scattering (Sec. II E). Den Hartog, Doughty, and Lawler[5] used anisotropic scattering for elastic collisions, isotropic scattering for excitation collisions, and either isotropic or the above anisotropic scheme for ionization collisions. Their results (He discharge: 3.5 torr, 0.62 cm electrode gap) indicate that the inelastic rates agree fairly well at the lowest voltage (173 V). However, at the highest voltage (600 V), the as-

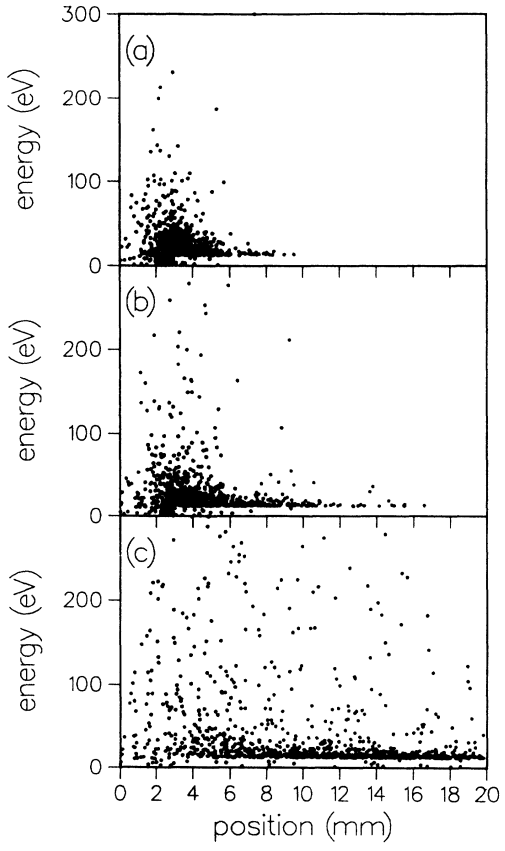

FIG. 12. Snapshot of energy and position of electrons for different scattering assumptions. $E(x)$ and $j_{be,\text{cathode}}$ are from the solution to the multibeam model at 275 V and 0.6 torr: (a) isotropic scattering; (b) anisotropic scattering; (c) full forward scattering.

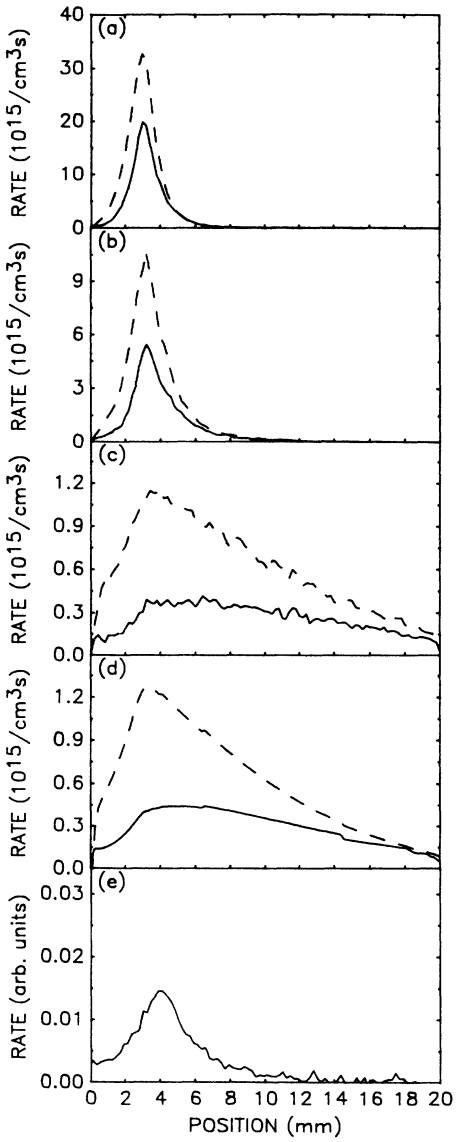

FIG. 13. Comparison of the effect of different scattering assumptions on ionization (dashed line) and excitation (solid line) rates. $E(x)$ and $j_{be,\text{cathode}}$ are from the solution to the multibeam model at 275 V and 0.6 torr. (a) isotropic scattering; (b) anisotropic scattering; (c) full forward scattering; (d) multibeam (self-consistent); (e) experimental optical-emission (419.832 nm; $1s_4$-$3p_5$ in Paschen notation) profile at similar conditions.

sumption of isotropic ionization collisions results in inelastic rates almost a factor of 2 greater than for anisotropic scattering. The reason for the difference between the various predictions is most probably the degree of anisotropy applied to the various collision phenomena incorporated in the simulations. Nonetheless, the importance of anisotropic scattering is apparent in these systems.

The inelastic rates with pure forward scattering [Fig. 13(c)] and from the multibeam model [Fig. 13(d) are significantly different from the cases with angular scattering. It is reassuring to note that the profiles in Figs. 13(c) and 13(d) are essentially the same. This is to be expected, since the methods are similar.[23]

The similarity between the optical-emission measurement [Fig. 13(e)] and the anisotropic case indicates that angular scattering of fast electrons is important.

B. Self-consistent hybrid particle-fluid simulation

In Fig. 14 we present preliminary results from a self-consistent simulation of the discharge with a particle representation of fast electrons. The conditions are 275 V and 0.6 torr, and γ is 0.3. Comparison to the multibeam results (Fig. 10) indicates that species density profiles [Fig. 14(a)] are more asymmetric. This is a direct consequence of inelastic rates [Fig. 14(c)] being highly peaked at the cathode sheath edge ($\sim$2.6 mm). Furthermore, the predicted excitation rate is in agreement with the optical-emission measurement [Fig. 13(e)]. As in the beam models, we observe a field reversal slightly to the anode side of the maximum in species densities.

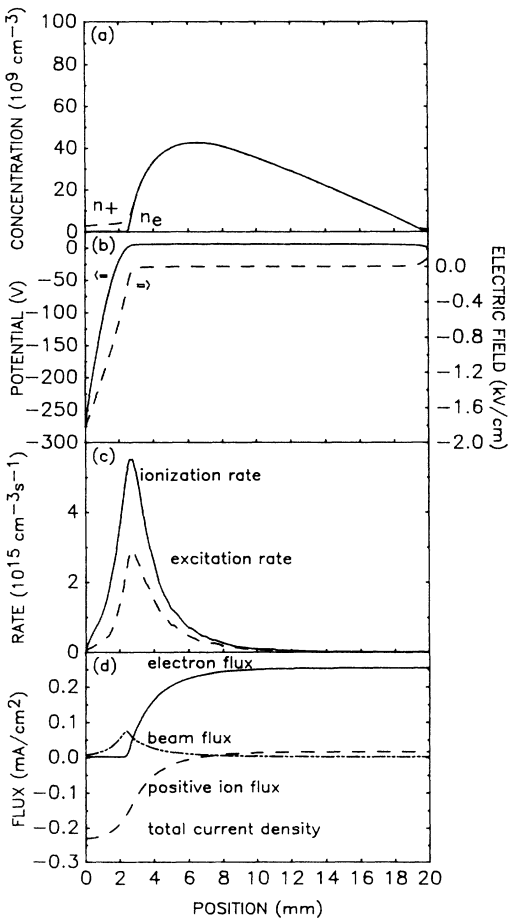

FIG. 14. Solution to the hybrid particle-fluid model: (a) slow-electron and ion densities; (b) potential and electric field; (c) inelastic rates; (d) charged particle fluxes and total current density. The conditions are 275 V and 0.6 torr. The field reversal occurs at 6.68 mm and the species density maximum is at 6.42 mm.

It is interesting to note that results from the single-beam model (Fig. 6) are fairly similar to results from this hybrid simulation. This agreement is fortuitious, arising from a cancellation of errors in the approximations built into the single-beam model. In some sense, the monoenergetic assumption reduces the impact of the high-energy tail present in the multibeam model that penetrates deep into the discharge.

VI. CONCLUSION

The single or monoenergetic beam model, while producing apparently correct results, displays some discrepancies when compared to the higher-order multibeam approach. The multibeam model, which is essentially a Boltzmann solution with the assumption of full forward scattering for fast electrons, is an improvement over the single-beam model. Nonetheless, comparisons with experimental optical-emission measurements reveal that the multibeam model predicts excitation profiles that extend too far into the discharge. Our Monte Carlo simulations of fast electrons indicate that the nature of fast-electron angular scattering is important for accurate model predictions. Finally, our results from the hybrid particle-fluid technique which include the effects of angular scattering demonstrate that it is possible to obtain self-consistent simulations of a dc discharge in which nonequilibrium fast-electron transport is included.

ACKNOWLEDGMENTS

The authors would like to acknowledge helpful discussions with R. A. Gottscho and I. J. Morey. This work was supported in part by the National Science Foundation Grant No. CBT-8707782, and the San Diego Supercomputer Center.

APPENDIX A: RELATIONSHIP OF THE MULTIBEAM METHOD TO THE BOLTZMANN EQUATION

The assumption of full forward scattering implies that the Boltzmann equation for a dc discharge between two infinitely wide parallel electrodes can be written as

$$v\frac{\partial f^*(x,v)}{\partial x}-\frac{eE(x)}{m_e}\frac{\partial f^*(x,v)}{\partial v}=\left[\frac{\partial f^*(x,v)}{\partial t}\right]_{\text{coll}}, \quad \text{(A1)}$$

where $f^*(x,v)$ is the electron velocity distribution function, and v is the velocity in the x direction.[45] Equation (A1) can be rewritten with (x,ε) as independent variables,

$$\frac{\partial[f(x,\varepsilon)\sqrt{2\varepsilon/m_e}]}{\partial x}-eE(x)\frac{\partial[f(x,\varepsilon)\sqrt{2\varepsilon/m_e}]}{\partial\varepsilon}=\left[\frac{\partial f(x,\varepsilon)}{\partial t}\right]_{\text{coll}}, \quad \text{(A2)}$$

where $f^*(x,v)dv=f(x,\varepsilon)d\varepsilon$, and $\varepsilon=m_e v^2/2$. The collision integral, $[\partial f(x,\varepsilon)/\partial t]_{\text{coll}}$, contains only contributions from excitation and ionization. Elastic scattering is not included because of the negligible energy transfer involved. Thus the collision integral can be expressed as follows:

$$\left[\frac{\partial f(x,\varepsilon)}{\partial t}\right]_{\text{coll}}=-n_n[\sigma_{\text{ion}}(\varepsilon)+\sigma_{\text{ext}}(\varepsilon)](2\varepsilon/m_e)^{1/2}f(x,\varepsilon)+n_n\sigma_{\text{ext}}(\varepsilon')(2\varepsilon'/m_e)^{1/2}f(x,\varepsilon')$$
$$+\int_{2\varepsilon+\varepsilon_{\text{ion}}}^{\infty}n_nS(\hat{\varepsilon},\varepsilon)(2\hat{\varepsilon}/m_e)^{1/2}f(x,\hat{\varepsilon})d\hat{\varepsilon}+\int_0^{\varepsilon}n_nS(\varepsilon',p)(2\varepsilon'/m_e)^{1/2}f(x,\varepsilon')dp\ , \quad \text{(A3)}$$

where ε' is the energy before collision ($\varepsilon'=\varepsilon+\varepsilon_{\text{ext}}$ for excitation, and $\varepsilon'=\varepsilon+\varepsilon_{\text{ion}}+p$ for ionization). Hence, substituting $J_{be}(x,\varepsilon)$ for $(2\varepsilon/m_e)^{1/2}f(x,\varepsilon)$, the Boltzmann equation can be written as follows:

$$\frac{\partial J_{be}(x,\varepsilon)}{\partial x}-eE(x)\frac{\partial J_{be}(x,\varepsilon)}{\partial\varepsilon}=-n_n[\sigma_{\text{ion}}(\varepsilon)+\sigma_{\text{ext}}(\varepsilon)]J_{be}(x,\varepsilon)+n_n\sigma_{\text{ext}}(\varepsilon+\varepsilon_{\text{ext}})J_{be}(x,\varepsilon+\varepsilon_{\text{ext}})$$
$$+\int_0^{\infty}n_nS(2\varepsilon+\varepsilon_{\text{ion}}+\tilde{\varepsilon},\varepsilon)J_{be}(x,2\varepsilon+\varepsilon_{\text{ion}}+\tilde{\varepsilon})d\tilde{\varepsilon}$$
$$+\int_0^{\varepsilon}n_nS(\varepsilon+\varepsilon_{\text{ion}}+p,p)J_{be}(x,\varepsilon+\varepsilon_{\text{ion}}+p)dp\ . \quad \text{(A4)}$$

Using the appropriate finite-difference approximations for the derivatives in Eq. (A4),

$$\frac{\partial J_{be}(x,\varepsilon)}{\partial x}=\frac{J_{be}(x_i+\Delta x_i,\varepsilon_k+\Delta\varepsilon)-J_{be}(x_i,\varepsilon_k+\Delta\varepsilon)}{\Delta x_i}\ , \quad \text{(A5a)}$$

and

$$\frac{\partial J_{be}(x,\varepsilon)}{\partial\varepsilon}=\frac{J_{be}(x_i,\varepsilon_k+\Delta\varepsilon)-J_{be}(x_i,\varepsilon_k)}{\Delta\varepsilon}\ , \quad \text{(A5b)}$$

and if Δx_i is chosen such that $-eE(x_i)\Delta x_i=\Delta eV_i=\Delta\varepsilon$, we obtain the next equation:

$$J_{be}(x_i+\Delta x_i,\varepsilon_k+\Delta eV)=J_{be}(x_i,\varepsilon_k)-\Delta x_i n_n[\sigma_{\text{ion}}(\varepsilon_k)+\sigma_{\text{ext}}(\varepsilon_k)]J_{be}(x_i,\varepsilon_k)$$
$$+\Delta x_i n_n\sigma_{\text{ext}}(\varepsilon_k+\varepsilon_{\text{ext}})J_{be}(x_i,\varepsilon_k+\varepsilon_{\text{ext}})$$
$$+\Delta x_i n_n\sum_{\varepsilon_n=0}^{\infty}S(2\varepsilon_k+\varepsilon_{\text{ion}}+\varepsilon_n,\varepsilon_k)J_{be}(x_i,2\varepsilon_k+\varepsilon_{\text{ion}}+\varepsilon_n)\Delta\varepsilon$$
$$+\Delta x_i n_n\sum_{p_j=0}^{\varepsilon_k}S(\varepsilon_k+\varepsilon_{\text{ion}}+p_j,p_j)J_{be}(x_i,\varepsilon_k+\varepsilon_{\text{ion}}+p_j)\Delta p\ . \quad \text{(A6)}$$

Note that we have replaced the integrals in Eq. (A4) with summations in the above equation. For small values of $\Delta x_i/\lambda_{\text{in}}(\varepsilon_k)$, $\Delta J_{be}(x_i,\varepsilon_k)$ in Eq. (13) can be approximated by

$$\Delta J_{be}(x_i,\varepsilon_k)=\frac{\Delta x_i J_{be}(x_i,\varepsilon_k)}{\lambda_{\text{in}}(\varepsilon_k)}=\Delta x_i n_n[\sigma_{\text{ion}}(\varepsilon_k)+\sigma_{\text{ext}}(\varepsilon_k)]J_{be}(x_i,\varepsilon_k)\ , \quad \text{(A7a)}$$

or

$$\Delta J_{be,\text{ion}}(x_i,\varepsilon_k)=\Delta x_i n_n\sigma_{\text{ion}}(\varepsilon_k)J_{be}(x_i,\varepsilon_k)\ , \quad \text{(A7b)}$$

and

$$\Delta J_{be,\text{ext}}(x_i,\varepsilon_k)=\Delta x_i n_n\sigma_{\text{ext}}(\varepsilon_k)J_{be}(x_i,\varepsilon_k)\ . \quad \text{(A7c)}$$

Substitution of the above equations into Eq. (A6) and setting $\Delta p=\Delta\varepsilon=1$ eV results in the multibeam equation [Eq. (16)].

Thus the multibeam approach of Carman and Maitland[23] is the same as solving the Boltzmann equation with the assumption of full forward scattering provided than $\Delta x_i/\lambda_{\text{in}}(\varepsilon_k)$ is sufficiently small. This ratio is less than 0.1 in all our simulations.

APPENDIX B: ION AND SLOW-ELECTRON CREATION RATES FROM THE MULTIBEAM MODEL

Since slow electrons are not created in the cathode fall, $C_e(x_i)$ in Eq. (2) is zero. $C_+(x_i)$ in Eq. (3) is given by

$$C_+(x_i)\Delta x_i = \sum_{\varepsilon_k=18}^{\infty} \Delta J_{be,\text{ion}}(x_i,\varepsilon_k) \ . \tag{B1}$$

$C_e(x_i)$ in the negative glow is given by the following expression:

$$C_e(x_i)\Delta x_i = \sum_{\varepsilon_k=1}^{12} \Delta J_{be,\text{en}}(x_i,\varepsilon_k) + \sum_{\varepsilon_k=13}^{24} \Delta J_{be,\text{ext}}(x_i,\varepsilon_k) + \sum_{\varepsilon_k=42}^{\infty} \sum_{p_j=1}^{12} \Delta J_{be,\text{ion}}(x_i,\varepsilon_k) \frac{S(\varepsilon_k,p_j)}{\sigma_{\text{ion}}(\varepsilon_k)}$$
$$+ \sum_{\varepsilon_k=18}^{41} \Delta J_{be,\text{ion}}(x_i,\varepsilon_k) + \sum_{\varepsilon_k=30}^{40} \Delta J_{be,\text{ion}}(x_i,\varepsilon_k) \left[1 - \sum_{p_j=1}^{\varepsilon_k-29} \frac{S(\varepsilon_k,p_j)}{\sigma_{\text{ion}}(\varepsilon_k)} \right] + \sum_{\varepsilon_k=18}^{29} \Delta J_{be,\text{ion}}(x_i,\varepsilon_k) \ . \tag{B2}$$

The first term in Eq. (B2) corresponds to the electrons that are transferred to the slow group at the collision rate (discussed in Sec. II C). The second term represents the electrons that enter the slow group after an excitation collision. The third and fourth terms account for the progeny electrons that have energies less than or equal to ε_{ext}. The last two terms describe the electrons that enter the slow group because they have insufficient energy to remain in the fast group after an ionization collision.

[1] M. J. Druyvesteyn and F. M. Penning, Rev. Mod. Phys. **12**, 87 (1940).

[2] D. A. Doughty, E. A. Den Hartog, and J. E. Lawler, Phys. Rev. Lett. **58**, 2668 (1987).

[3] D. A. Doughty and J. E. Lawler, J. Appl. Phys. **45**, 611 (1984).

[4] J. R. Shoemaker, B. N. Ganguly, and A. Garscadden, Appl. Phys. Lett. **52**, 2019 (1988).

[5] E. A. Den Hartog, D. A. Doughty, and J. E. Lawler, Phys. Rev. A **38**, 2471 (1988).

[6] T. J. Sommerer, J. E. Lawler, and W. N. G. Hitchon, J. Appl. Phys. **64**, 1775 (1988).

[7] T. J. Sommerer, W. N. G. Hitchon, and J. E. Lawler, Phys. Rev. A **39**, 6356 (1989).

[8] J. P. Boeuf and P. Segur, in *Interactions Plasma Froids Matreiaux,* edited by C. Lejeune (Les Editions de Physique, 1988), p. 113.

[9] A. L. Ward, J. Appl. Phys. **33**, 2789 (1962).

[10] D. B. Graves and K. F. Jensen, IEEE Trans. Plasma Sci. **PS-14**, 78 (1986).

[11] P. Bayle, J. Vacquie, and M. Bayle, Phys. Rev. A **34**, 360 (1986).

[12] J. P. Boeuf, J. Appl. Phys. **63**, 1342 (1988).

[13] W. H. Long, Northrop Research and Technical Center Report No. AFAPL-TR-79-2038, 1979 (unpublished).

[14] P. Segur, M. Yousfi, J. P. Boeuf, E. Marode, A. J. Davies, and J. G. Evans, in *Electrical Breakdown and Discharges in Gases,* Vol. 89A of *NATO Advanced Study Institute, Series B: Physics,* edited by E. E. Kunhardt and L. H. Luessen (Plenum, New York, 1983), p. 331.

[15] N. A. Tran, E. Marode, and P. C. Johnson, J. Phys. D **10**, 2317 (1977).

[16] J. P. Boeuf and E. Marode, J. Phys. D **15**, 2169 (1982).

[17] M. Ohuchi and T. Kubota, J. Phys. D **16**, 1705 (1983).

[18] N. Sato and H. Tagashira, J. Phys. D **18**, 2451 (1985).

[19] T. J. Moratz, L. C. Pitchford, and J. N. Bardsley, J. Appl. Phys. **61**, 2146 (1987).

[20] R. A. Gottscho, A. Mitchell, G. R. Scheller, Y. Chan, and D. B. Graves, Phys. Rev. A **40**, 6407 (1989).

[21] A. V. Phelps, B. M. Jelenkovic, and L. C. Pitchford, Phys. Rev. A **36**, 5327 (1987).

[22] L. Friedland and Y. M. Kagan, J. Phys. D **15**, 1721 (1982).

[23] R. J. Carman and A. Maitland, J. Phys. D **20**, 1021 (1987).

[24] Y. M. Kagan, J. Phys. D **18**, 1113 (1985).

[25] B. Shi, J. Meyer, Z. Yu, and G. J. Collins, IEEE Trans. Plasma Sci. **PS-14**, 523 (1986).

[26] J. E. Lawler, Phys. Rev. A **32**, 2977 (1985).

[27] J. P. Boeuf, Phys. Rev. A **36**, 2782 (1987).

[28] M. S. Barnes, T. J. Cotler, and M. E. Elta, J. Comput. Phys. **77**, 53 (1988).

[29] A. D. Richards, B. E. Thompson, and H. H. Sawin, Appl. Phys. Lett. **50**, 492 (1987).

[30] L. Vuskovic and M. V. Kurepa, J. Phys. B **9**, 837 (1976).

[31] H. S. W. Massey and E. H. S. Burhop, *Collisions of Electrons with Atoms,* Vol. 1 of *Electronic and Ionic Impact Phenomena* (Clarendon, Oxford, 1969), Chap. 5.

[32] E. Eggarter, J. Chem. Phys. **62**, 833 (1975).

[33] L. R. Peterson and J. E. Allen, Jr., J. Chem. Phys. **56**, 6068 (1972).

[34] M. Hayashi, Institute of Plasma Physics, Nagoya University Report No. IPPJ-AM-19, 1981 (unpublished).

[35] J. E. Lawler (personal communication).

[36] A. V. Phelps and L. C. Pitchford, Phys. Rev. A **31**, 2932 (1985).

[37] E. W. McDaniel, *Collision Phenomena in Ionized Gases* (Wiley, New York, 1964), p. 469.

[38] L. S. Frost, Phys. Rev. **105**, 354 (1957).

[39] T. J. Moratz, J. Appl. Phys. **63**, 2558 (1988).

[40] S. L. Lin and J. N. Bardsley, J. Phys. B **8**, L461 (1975).

[41] C. K. Birdsall and A. B. Langdon, *Plasma Physics via Computer Simulation* (McGraw-Hill, New York, 1985).

[42] R. W. Boswell and I. J. Morey, Appl. Phys. Lett. **52**, 21 (1988).

[43] Y. Sakai, H. Tagashira, and S. Sakamoto, J. Phys. D **10**, 1035 (1977).

[44] E. DeMarinis, A. Sasso, and E. Arimondo, J. Appl. Phys. **63**, 649 (1988).

[45] T. Holstein, Phys. Rev. **70**, 367 (1946).

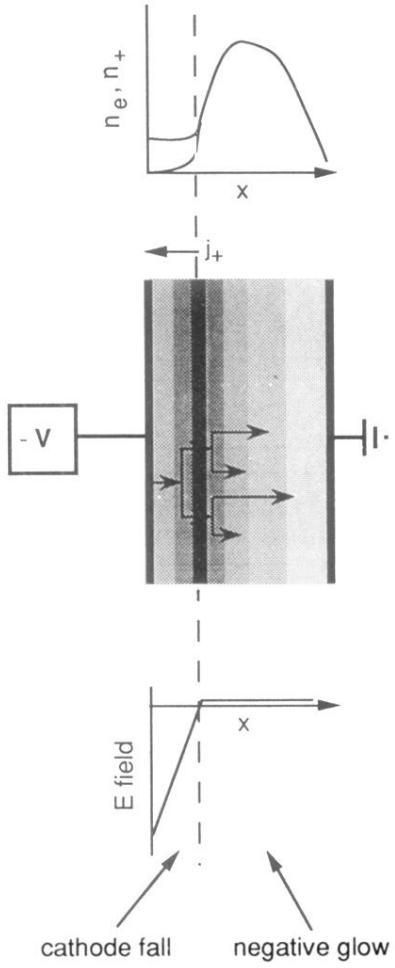

FIG. 1. Schematic of a dc discharge with typical density and electric field profiles. The shading intensity represents the intensity of light emission in the discharge.